Experimental studies on mechanical properties and ductile-to-brittle transition of ice-silica mixtures: Young's modulus, compressive strength, and fracture toughness

Yasui, Minami
Schulson, Erland M.
Renshaw, Carl E.

(Citation)
Journal of Geophysical Research. Solid Earth,122(8):6014-6030

(Issue Date)
2017-08

(Resource Type)
journal article

(Version)
Version of Record

AGU PUBLICATIONS

JGR

Journal of Geophysical Research: Solid Earth

RESEARCH ARTICLE
10.1002/2017JB014029

Key Points:
- Transitional strain rate increased upon increasing the silica volume fraction f for $f \leq 0.18$
- Fracture toughness increased upon increasing the silica volume fraction for $f \leq 0.34$ and scaled as $f^{0.5}$
- Young's modulus increased linearly with silica volume fraction for $f \leq 0.34$. Poisson's ratio (~0.33) was independent of f over this range

Supporting Information:
- Supporting Information S1

Correspondence to:
M. Yasui,
minami.yasui@pearl.kobe-u.ac.jp

Citation:
Yasui, M., E. M. Schulson, and C. E. Renshaw (2017), Experimental studies on mechanical properties and ductile-to-brittle transition of ice-silica mixtures: Young's modulus, compressive strength, and fracture toughness, *J. Geophys. Res. Solid Earth*, *122*, 6014–6030, doi:10.1002/2017JB014029.

Received 25 JAN 2017
Accepted 14 JUL 2017
Accepted article online 18 JUL 2017
Published online 9 AUG 2017

Experimental studies on mechanical properties and ductile-to-brittle transition of ice-silica mixtures: Young's modulus, compressive strength, and fracture toughness

Minami Yasui[1,2], Erland M. Schulson[2], and Carl E. Renshaw[2,3]

[1]Graduate School of Science, Kobe University, Hyogo, Japan, [2]Thayer School of Engineering, Dartmouth College, Hanover, New Hampshire, USA, [3]Department of Earth Sciences, Dartmouth College, Hanover, New Hampshire, USA

Abstract We measured Young's modulus, fracture toughness, and compressive strength of ice and of ice-0.25-μm hard silica bead mixtures in controlled systematic experiments to determine the effect of silica on the ductile-to-brittle transition. Unconfined compressive strength was measured in a cold room at −10°C under a constant strain rate ranging from 10^{-5} to 6×10^{-1} s^{-1} of mixtures with silica volume fraction f of 0, 0.06, and 0.18. In the brittle regime, the compressive strength σ_{peak} was a maximum at the transitional strain rate and then decreased with increasing strain rate. In the ductile regime, the σ_{peak} increased exponentially with increasing strain rate $\dot{\varepsilon}$ as $\dot{\varepsilon} = B \cdot \sigma_{peak}^{n}$. The stress exponent n for $f = 0.06$ and 0.18 was ~6, twice as large as the value of pure ice, $n \sim 3$. The transitional strain rate increased with increasing silica volume fraction; 10^{-3}–10^{-2} s^{-1} for pure ice, 10^{-2}–10^{-1} s^{-1} for $f = 0.06$, and $>6 \times 10^{-1}$ s^{-1} for $f = 0.18$. Fracture toughness and Young's modulus were measured over the range $0 \leq f \leq 0.34$. Fracture toughness scaled as $f^{0.5}$, while Young's modulus increased linearly with f. Finally, a theoretical model of the transitional strain rate proposed by Schulson (1990) and Renshaw and Schulson (2001) was compared to the measured transitional strain rates. Model predictions were in accord with measured transitional strain rates for pure ice but somewhat higher than observed for ice-silica mixtures. Large model uncertainty was due to high sensitivity of the transitional strain rate to the stress exponent n.

1. Introduction

Water ice is one of the most common materials on the surfaces of Earth, Mars, and many icy bodies such as icy satellites of jovian planets, comets, and Edgeworth-Kuiper-belt objects. In many cases it is mixed with rocky debris. For example, in glacial and periglacial environments of Earth, water ice is mixed with up to nearly 1% rocky debris [*Moore*, 2014]. The dwarf planet, Ceres, is thought to have a crust composed of an ice-rock mixture with the mass fraction of H_2O ice estimated to be approximately 17–30% [*McCord and Sotin*, 2005; *De Sanctis et al.*, 2015]. Assuming a rock density of ~3000 kg m^{-3}, the equivalent volume fraction of rocky materials of Ceres is 53–66%. The densities of icy satellites, as revealed by several spacecraft and ground-based observations, also indicate the presence of debris. For example, the densities of small-to-middle Saturnian icy satellites (diameter $<$ 800 km) determined by the Cassini spacecraft range from 340 to 1640 kg m^{-3}, suggesting that they are mixtures of ice, rock, and porosity [*Thomas*, 2010]. On Earth and elsewhere various landforms related to the flow and the fracture of ice-rock mixtures are found. Examples include glaciers and ice sheets on Earth, various fretted terrains such as lobate debris aprons on Mars [e.g., *Squyres*, 1989], relaxed craters and global ridge, and trough terrains such as grooves on Ganymede and bands on Europa. To clarify the formation processes and structures of these and other tectonic features, it is necessary to understand the rheological properties of ice-rock mixtures over a range of physical and environmental conditions.

The rheological properties of water ice such as compressive strength, viscosity, and the flow law have been studied extensively in relation to engineering, glaciology, and planetary science. Recently, the flow law of ice-rock mixtures has been studied through laboratory experiments, field observations, and numerical models, under both terrestrial conditions (at temperatures higher than −20°C and under 1 atm) as summarized in the paper of *Moore* [2014 and references therein], and also under extraterrestrial conditions (at very low temperature and/or under high confining pressure) [e.g., *Durham et al.*, 1992; *Mangold et al.*, 2002]. In these works, investigators used various rocky materials of different sizes and shapes and found that the compressive strength and the viscosity increased with an increase in rock content.

In contrast, the brittle behavior of ice-rock mixtures, and particularly the ductile-to-brittle transition, is less clear. This transition strongly affects the behavior of the sea ice cover on the Arctic Ocean [*Schulson*, 2004] and the tectonic style, flow features, and fracture patterns on the surfaces of icy bodies [e.g., *Nimmo*, 2004; *Dombard and McKinnon*, 2006]. *Schulson* [1990] proposed a theoretical model for the strain rate corresponding to the ductile-to-brittle transition by considering the competition at the tips of cracks between stress relaxation via creep and stress concentration. He showed that the theoretical transitional strain rate predicted by this model matched that obtained in laboratory experiments on freshwater ice. The model and experimental observations indicate that the critical transitional strain rate depends on a number of factors including grain size [*Batto and Schulson*, 1993], temperature [*Qi and Schulson*, 1998; *Arakawa and Maeno*, 1997], and confining pressure [*Durham et al.*, 1983; *Kirby et al.*, 1985]. Subsequently, *Renshaw and Schulson* [2001] showed that the model accounts as well for the ductile-to-brittle transition in a variety of rock and minerals loaded under confinement.

In the case of ice-rock mixtures, there are only a few studies on the ductile-to-brittle transition. *Mangold et al.* [2002] performed compression experiments on ice-quartz sand mixtures with a sand diameter of 0.05–2 mm under a constant stress of 14.0-20.9 MPa and constant temperature of −10°C under a confining pressure of 12 MPa and found that the ductile-to-brittle transition occurred at the sand volume fraction of 0.65–0.75; at higher sand volume fractions, brittle failure occurred. *Durham et al.* [2009] performed compression experiments on ice-sand mixtures under a constant stress of 11–53 MPa and constant temperature of −50 or −30°C under a confining pressure of 60–200 MPa and found that the volume fraction of sand that marks the ductile-to-brittle transition corresponded to the most closely packed arrangement of sand particles in the mixture, independent of both temperature and confining pressure. In these previous works, the critical sand content marking the ductile-to-brittle transition was determined under the condition of constant stress. Unclear, however, is the critical transitional strain rate under constant sand content. The only existing such study for ice-rock mixtures is that by *Yasui and Arakawa* [2008]. They performed compression experiments on mixtures of ice-1-μm-silica beads with silica volume fraction of 0 to 0.63, at constant strain rate from 9×10^{-7} to 3×10^{-3} s^{-1} and constant temperature from −25 to −10°C. *Yasui and Arakawa* [2008] found that the critical transitional strain rates, $\dot{\varepsilon}_{D/B}$, for high silica volume fractions of 0.29 and 0.63 were essentially the same, irrespective of silica volume fraction, and that it could be expressed as $\dot{\varepsilon}_{D/B}\left[s^{-1}\right] = A_{D/B}\exp\left(-E_{D/B}/R'T\right)$, where R' is the gas constant and T is the temperature and $A_{D/B}$ and $E_{D/B}$ are constants ($A_{D/B}$=1.62 × 10^{15} s^{-1} and $E_{D/B}$=95.6 kJ mol^{-1}), giving $\dot{\varepsilon}_{D/B} = 1.6 \times 10^{-4}$ s^{-1} at −10°C. However, they did not find the transitional strain rate for lower silica volume fractions. When strained at rates up to 3×10^{-3} s^{-1}, the low-silica mixtures exhibited ductile behavior. Here we report the transitional strain rate $\dot{\varepsilon}_{D/B}$ of ice at −10°C over a lower range of silica content (0–18%).

Specifically, we carried out compression experiments on ice-silica mixtures with silica volume fraction lower than 0.2 over a range of strain rate wider than that explored by *Yasui and Arakawa* [2008]. The principal objective was to investigate the effect of silica content on the transitional strain rate. To provide a framework for interpreting the results, we compare the experimentally observed transitional strain rates to predictions of the model proposed earlier [*Schulson*, 1990; *Renshaw and Schulson*, 2001].

2. Experimental Methods

2.1. Sample Preparation

Following the procedure described elsewhere [*Yasui and Arakawa*, 2008], samples were prepared by mixing ice grains/seeds with commercial silica beads, in a cold room at −10°C in the Ice Research Laboratory, Dartmouth College. Ice grains/seeds were produced by crushing pure freshwater ice that was produced by freezing deionized water and then by sieving to select the grains smaller than 850 μm in diameter. The silica beads were a high-purity synthesis of spherical silica (>99.8% SiO_2; Admatechs Company Ltd.), with a narrow particle size distribution to exclude possible effects of bead size and shape: the bead diameter corresponding to the peak of size distribution is 0.25 μm. The density of the silica bead is 2200 kg m^{-3}.

We varied systematically the silica volume fraction of the sample, f. For the compression experiments to examine the ductile-to-brittle transition, we made mixtures of f = 0, ~0.06, and ~0.18. For three-point bending tests to examine the fracture toughness and for ultrasonic velocity measurements to examine the elastic properties, we made mixtures of f = 0, ~0.06, ~0.12, ~0.18, and ~0.34. In this paper, we term the mixture of ice and silica beads "silica ice" to distinguish it from silica-free ice which we term "pure ice." The porosity of

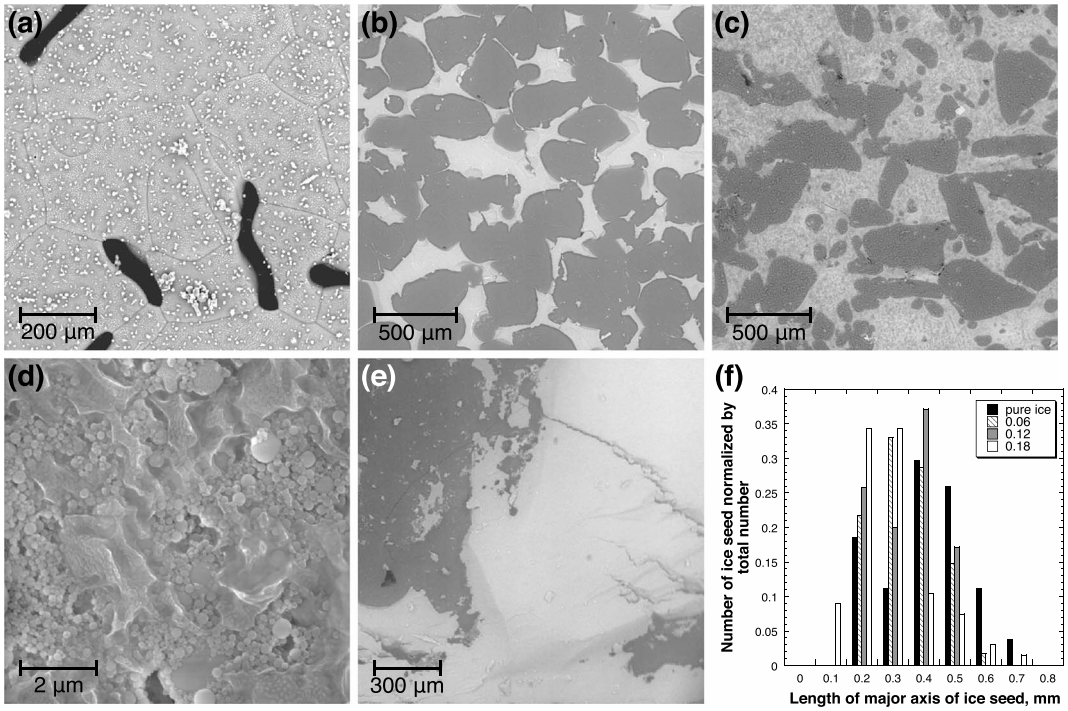

Figure 1. SEM images in BSE mode. (a) Pure ice. The small white jagged clusters on the surface of ice grains are frost generated by the vacuum in the SEM sample room. The long black areas indicate pores. (b) Silica ice with silica volume fraction $f = 0.06$. (c) Silica ice with $f = 0.18$. (d) Enlarged image of white area in Figure 1c. (e) Silica ice with $f = 0.34$. The black areas and white areas in Figures 1b, 1c, and 1e indicate ice grains and fine composite matrix composed of silica beads and frozen water, respectively. (f) Size frequency distribution of ice seed analyzed by using SEM images.

all samples before testing was below ~5%, as determined from measurements of volume and mass: 5.0 ± 1.7% for pure ice, 2.2 ± 1.1% for f = 0.06, 2.4 ± 0.9% for f = 0.12, 3.9 ± 2.1% for f = 0.18, and 0.7 ± 0.7% for f = 0.34. The number before the "plus-minus sign" means the median value of all samples having same silica volume fraction, and the number beyond "plus-minus sign" means the difference between the median value and the maximum (or the minimum) value.

The samples were made as follows: For the lower silica mixture ($f \leq 0.18$), ice grains/seeds were homogeneously mixed with silica beads in a plastic bag, and then a small quantity (a few grams) of this mixture was put into a cylindrical mold of inside diameter 30 mm and of height 60 mm. The mold was then filled with a little distilled water at a temperature of 0°C to fill spaces and to reduce porosity as much as possible. This process was repeated (>15 times) until the contents filled the mold in order to assure homogenous distribution of silica beads. Subsequently, freezing occurred over a period of 1 day in a cold room set at −10°C. For the most silica-rich samples ($f = 0.34$), silica beads were first suspended in distilled water and then the suspension was frozen. These two preparation methods are same as those of *Yasui and Arakawa* [2008].

2.2. Microstructure

The microstructures of silica ice and pure ice were observed by using a scanning electron microscope (SEM), XL-30 ESEM-FEG (SEMTech Solutions) at the Electron Microscope Facility of Dartmouth College. Installed in the SEM was a cryogenic stage that operated at a temperature of −140 ± 2°C to reduce the sublimation of the surface. The specimen was made by using a microtome and a razor blade to create a fresh surface. Figure 1 shows SEM images of pure ice and silica ices with f = 0.06, 0.18, and 0.34. In pure ice (Figure 1a), ice grains of a few hundreds of microns in diameter are evident along with long thin pores distributed along the ice grain boundaries. The distilled water that was added to fill the space between the grains served, upon freezing, to consolidate the seeds. In the case of silica ices with $f = 0.06$ and 0.18 (Figures 1b and 1c), two areas of different tone are observed. The darker-toned area indicates ice from the seed grains, while the lighter-toned area indicates a fine mixture of silica beads and ice (Figure 1d) that formed upon freezing the distilled water that was used to fill the spaces between the seed grains and the beads. This fine mixture tends to form

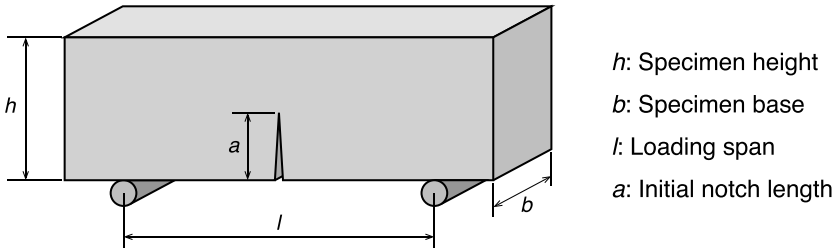

Figure 2. Schematic illustration for specimen dimension of three-point bending (mode-I loading) tests.

a matrix of silica ice, particularly for the higher silica contents of $f = 0.18$ (Figure 1c) and $f = 0.34$ (Figure 1e). The white area in Figure 1e is assumed to possess a microstructure similar to that of the fine mixture shown in Figure 1d. Silica ices for $f = 0.12$ had a similar microstructure to that for $f = 0.06$, but the white area was more extensive. In other words, the microstructural role of silica beads, as introduced in the manner in which we prepared our silica ices, is to form for low silica volume fraction ($f \leq 0.12$) a partial network-like silica/ice fine mixture surrounding some of the consolidated and matrix-forming ice seed grains. For higher silica contents ($f \geq 0.18$) the role of the silica beads is to form a matrix composed of the fine mixture of silica beads and ice in which the ice seed grains are distributed.

We measured the size of the ice grains/seeds (black areas in Figure 1) in from SEM images by using the sample without deformation and the software ImageJ. Each ice grain was fit by elliptic approximation and the length of major axis was measured. We measured 27 seeds in pure ice, 115 for $f = 0.06$, 35 for $f = 0.12$, and 67 for $f = 0.18$. The average lengths of the major axes with standard deviation were 0.36 ± 0.14 mm for pure ice, 0.30 ± 0.10 mm for $f = 0.06$ and 0.12, and 0.24 ± 0.12 mm for $f = 0.18$. Figure 1f shows the normalized size frequency distribution of ice seeds. In Figure 1f, the lengths of major axes corresponding to the peak of the frequency distribution were 0.3–0.4 mm for pure ice and $f = 0.12$, 0.2–0.3 mm for $f = 0.06$, and 0.1–0.2 mm for $f = 0.18$. Both lengths, the average length of the major axis and the length of major axis corresponding to the peak of the frequency distribution in Figure 1f, decreased gradually with increasing silica volume fraction.

2.3. Elastic Properties

The elastic properties, Young's modulus, E, Poisson's ratio, ν, and Shear modulus, G, were determined by measuring the ultrasonic velocities of both longitudinal and shear waves, using an ULT-100 ultrasonic velocity test system (GCTS Testing System). Measurements were made in a cold room at −10°C. The specimens had a diameter of 30 mm and a length of 55–61 mm. The specimens were put between two platens that included six sensors and the longitudinal and/or shear signals were run about 50 times between two platens so the average signal wave for the 50 waveforms was obtained. Each signal wave has a high level of acoustic noise, so a band-pass filter was set for both longitudinal and shear waves; the frequency range of the band-pass filter was 12 to 466 kHz for the longitudinal wave, and it was 39 to 347 kHz for the shear wave.

Young's modulus, E; Poisson's ratio, ν; and shear modulus, G, were determined from the relationships:

$$E = \rho {V_s}^2 \frac{3{V_l}^2 - 4{V_s}^2}{{V_l}^2 - {V_s}^2}, \tag{1}$$

$$\nu = \frac{1}{2} \frac{{V_l}^2 - 2{V_s}^2}{{V_l}^2 - {V_s}^2}, \tag{2}$$

$$G = \rho {V_s}^2, \tag{3}$$

where ρ is the specimen density and V_l and V_s are the longitudinal wave and the shear wave velocities, respectively.

2.4. Fracture Toughness

Fracture toughness was measured using the method of three-point bending (mode-I loading), following ASTM-E399 [*ASTM E399*, 2009]. The specimens were shaped by cutting the original cylindrical silica ice and pure ice by a band-saw and a microtome. The specimens had a rectangular parallelepiped shape with the specimen base, b, of 12–19 mm and the specimen height, h, of 10–18 mm, as illustrated in Figure 2. We initially varied the specimen length between either ~30 mm or ~60 mm to examine whether the loading span, l,

Table 1. Experimental Conditions and Results From Three-Point Bending Tests

Run Number	Silica Volume Fraction f [a]		h [b] (mm)	b [b] (mm)	l (mm)	a [b] (mm)	K_{Ic} (kPa m$^{1/2}$)
20160913-2	0	0	16.1 (0.2)	16.0 (0.2)	51	6.5 (0.03)	94.9
20160913-3		0	17.8 (0.2)	17.7 (0.1)	51	6.4 (0.4)	114.2
20160913-4		0	15.0 (0.2)	15.5 (0.2)	24	5.5 (0.3)	114.3
20160913-5		0	16.3 (0.1)	15.8 (0.2)	25	6.1 (0.1)	75.6
20161101-1	0.06	0.058	15.0 (0.1)	14.6 (0.04)	23	6.1 (0.1)	190.5
20161101-2		0.058	15.0 (0.1)	13.1 (0.1)	23	5.7 (0.4)	275.7
20161101-3		0.061	13.6 (0.1)	14.3 (0.1)	55	3.9 (0.5)	180.4
20161101-4		0.058	14.9 (0.1)	14.8 (0.03)	55	4.3 (0.3)	247.7
20161101-5	0.12	0.120	14.3 (0.1)	14.2 (0.1)	55	4.1 (0.4)	343.5
20161101-6		0.123	13.9 (0.1)	13.7 (0.1)	55	4.3 (0.1)	303.0
20161101-7		0.127	13.5 (0.1)	13.5 (0.1)	52	4.8 (0.2)	302.0
20161102-1		0.121	13.3 (0.1)	13.6 (0.03)	24	5.5 (0.1)	329.2
20160916-1	0.18	0.186	10.3 (0.1)	14.3 (0.4)	23	7.3 (0.3)	370.8
20160916-2		0.184	11.3 (0.02)	12.4 (0.01)	23	7.0 (0.1)	270.5
20160916-3		0.190	11.9 (0.1)	17.3 (0.2)	23	6.0 (0.02)	204.8
20160919-1		0.190	11.9 (0.2)	16.4 (0.1)	23.5	6.0 (0.02)	307.9
20160919-2		0.192	12.4 (0.2)	19.2 (0.01)	23.5	6.1 (0.1)	375.7
20160919-3		0.184	16.9 (0.03)	12.2 (0.1)	23.5	8.2 (0.01)	337.0
20161101-8	0.34	0.336	13.1 (0.4)	13.4 (0.3)	53	7.1 (0.03)	225.5
20161101-9		0.336	13.9 (0.3)	13.0 (0.5)	55	6.6 (0.4)	474.6
20161101-10		0.336	12.4 (0.3)	11.9 (0.2)	50	6.9 (0.1)	404.4
20161101-11		0.336	12.6 (0.2)	13.1 (0.4)	50	6.4 (0.1)	483.2

[a]Left side: silica volume fraction used in the text. Right side: silica volume fraction measured before each test.
[b]The numbers in parentheses give the standard deviation.

affects the fracture toughness. The fracture toughness did not change with l. Thus, l was set to be 23–25 mm for the shorter specimens and 50–55 mm for the longer specimens. For samples with silica volume fractions from 0 to 0.18 the notch was made by cutting at the center of basal surface between two loading points with a razor blade having the thickness of 0.15 mm. The blade was very thin so the notch was sharp. In the case of $f = 0.34$, the notch was made with a knife having the thickness of 1 mm, resulting in a notch of included angle $<15°$. The initial notch length, a, was changed from 3 to 8 mm. Thus, the ratio, a/h, was changed from 0.3 to 0.7. This ratio did not systematically affect the derived value of fracture toughness. The experimental conditions for each sample are shown in Table 1.

Three-point bending test is one of the standard tests to measure mechanical properties such as fracture toughness. The specimen was placed on two supporting bars (a set span of l), and a force was loaded at the center of top surface of specimen until the specimen broke. In our experiments, a string connected to a bucket was hung up from the above specimen and water was poured into the bucket until specimen failure. To calculate the load at failure, we measured the weight of water poured into the bucket. We performed the bending tests for specimens with the same silica volume fraction at 4–6 times to determine reproducibility.

The specimens were loaded in a cold room at the temperature of −10°C at a constant loading rate. We measured the time required to pour the water into the bucket and calculated the loading rate from this pouring time and the weight of the water. To eliminate contributions from creep deformation, the loading rate at −10°C should be >0.3–10 kPa m$^{1/2}$ s^{-1} for pure ice [*Nixon and Schulson*, 1987]. In the case of silica ice, the critical loading rate is unclear, but given that silica ice creeps more slowly than pure ice, the limit is expected to be lower than that of pure ice. In the experiments reported here, the loading rate always exceeded 10 kPa m$^{1/2}$ s^{-1}.

Fracture toughness was computed from the relationship [*ASTM E399*, 2009]:

$$K_{Ic} = \frac{Pl}{bh^{3/2}} f(d), \tag{4}$$

where P is the load at failure and $f(d)$ is a function including the term of a/h and is given by the relationship:

$$f(d) = 3\sqrt{d}\,\frac{1.99 - d(1-d)\left(2.15 - 3.93d + 2.7d^2\right)}{2(1+2d)(1-d)^{3/2}}, \tag{5}$$

where $d = a/h$.

Table 2. Experimental Conditions and Results From Uniaxial Compression Tests

Run Number[a]	Silica Volume Fraction f[b]	Porosity (%)	Strain Rate (s^{-1})	Peak Stress (MPa)	Deformation Behavior[c]
20160510-1*	0	0	3.7	9.99×10^{-6}	2.51	D
20160510-2		0	3.7	1.00×10^{-4}	4.70	D
20160516-1*		0	4.1	1.00×10^{-4}	4.93	D
20160517-1		0	4.2	9.98×10^{-6}	2.56	D
20160527-1*		0	3.9	1.00×10^{-3}	6.30	D
20160527-2		0	4.6	1.00×10^{-2}	7.66	B
20160627-2		0	4.7	1.02×10^{-1}	3.56	B
20160706-1		0	4.4	5.66×10^{-1}	3.63	B
20160706-2*		0	5.1	5.89×10^{-1}	2.96	B
20160706-3*		0	6.7	9.98×10^{-2}	4.95	B
20160706-4*		0	3.4	1.01×10^{-2}	11.04	B
20160707-1		0	3.5	1.00×10^{-3}	7.26	D
20161110-1	0.06	0.054	1.9	1.01×10^{-2}	9.42	D
20161110-2*		0.057	1.4	1.01×10^{-2}	14.48	D
20161110-3		0.057	2.1	1.01×10^{-1}	9.53	B
20161110-4*		0.060	1.1	1.01×10^{-1}	16.52	B
20161111-1*		0.055	3.1	5.05×10^{-1}	9.53	B
20161111-2		0.055	3.1	5.49×10^{-1}	5.80	B
20161123-1*		0.056	1.8	1.00×10^{-3}	8.82	D
20161123-2*		0.057	1.7	1.00×10^{-4}	6.33	D
20161123-3*		0.053	2.0	1.00×10^{-5}	4.06	D
20161201-1		0.054	2.4	1.00×10^{-3}	8.96	D
20161201-2		0.055	1.9	1.00×10^{-4}	6.35	D
20161201-3		0.057	2.1	1.00×10^{-5}	4.12	D
20160518-1*	0.18	0.169	2.3	1.00×10^{-5}	4.80	D
20160518-2*		0.172	2.3	1.00×10^{-4}	6.32	D
20160527-3*		0.170	2.3	1.00×10^{-3}	8.59	D
20160602-1		0.178	3.9	1.01×10^{-2}	12.09	D
20160627-1*		0.190	2.2	1.02×10^{-1}	18.20	D
20160701-1*		0.187	5.9	5.99×10^{-1}	22.68	D
20160701-2		0.187	1.8	5.71×10^{-1}	27.39	D
20160707-2		0.175	2.9	1.00×10^{-3}	7.95	D
20160707-3*		0.183	3.7	1.01×10^{-2}	11.73	D
20160708-1		0.183	2.9	1.00×10^{-5}	4.72	D
20161205-1		0.188	4.6	1.00×10^{-4}	5.32	D
20161205-2		0.190	3.7	1.02×10^{-1}	12.95	D

[a] Asterisk (*) indicates the results shown in Figures 3 and 4.
[b] Left side: silica volume fraction used in the text. Right side: silica volume fraction measured before each test.
[c] "D" means ductile behavior, and "B" means brittle behavior determined from the stress-strain curve (Figures 3 and S1), the macroscopic appearance of deformed sample (Figure 4), and the peak stress behavior (Figure 5).

2.5. Compressive Strength and Ductile-to-Brittle Transition

We conducted unconfined uniaxial compression experiments under constant strain rates by using in uniaxial mode a multiaxial servo-hydraulic testing machine (MTS Systems Corp.) situated in a cold room in the Ice Research Laboratory at Dartmouth College. The room temperature was set to be −10°C. The strain rate ranged from 10^{-5} to 6.0×10^{-1} s^{-1}. The samples had a cylindrical shape with a diameter of 30 mm and a height of 60 mm for the strain rates of 10^{-5}–10^{-1} s^{-1}; for the highest strain rate of 6.0×10^{-1} s^{-1}, the sample length was reduced to 30 mm. The experimental conditions for each sample are shown in Table 2. Prior to testing, the specimens were milled to improve the degree of parallelism of the ends. To reduce friction, thin polyethylene sheet was placed at the ice/platen interface.

Schulson [1990] and *Renshaw and Schulson* [2001] created a physical model of the ductile-to-brittle transition that accounts for the effects of strain rate, temperature, grain size, etc., in terms of the competition between stress buildup and stress relaxation via creep at the tips of cracks [see *Schulson and Duval*, 2009, Chapter 13]. The model incorporates the assumption that stress-relaxation occurs via power law or dislocation creep, as is appropriate for bodies deformed at relatively high homologous temperatures under relatively high stresses. Under such conditions, the ductile-to-brittle transition, when expressed in terms

of a critical transitional strain rate, $\dot{\varepsilon}_{D/Bcal}$, defined under compressive loading as follows [*Schulson and Duval*, 2009]:

$$\dot{\varepsilon}_{D/Bcal} = \frac{(n+1)^2(3)^{(n-1)/2}BK_{Ic}{}^n}{n\sqrt{\pi}[(1-R)-\mu(1-R)]c^{n/2}} \quad (\mu < 1), \tag{6}$$

where K_{Ic} is the fracture toughness, μ is the coefficient of kinetic friction, c is the half length of the initial crack within the material, R is the ratio of two principal compressive stresses, σ_3/σ_1 (σ_1 is the highest and σ_3 is the least compressive stress, where compressive stress is taken to be a positive quantity), and B and n are constants in the power law relationship that describes creep, $\dot{\varepsilon} = B \cdot \sigma^n$ (σ is the effective stress and $\dot{\varepsilon}$ is the strain rate). In this study, we performed uniaxial compression tests, so $\sigma_3 = 0$ and $R = 0$. Thus, equation (6) can be written as

$$\dot{\varepsilon}_{D/Bcal} = \frac{(n+1)^2(3)^{(n-1)/2}BK_{Ic}{}^n}{n\sqrt{\pi}(1-\mu)c^{n/2}} \quad (\mu < 1), \tag{7}$$

We applied the model in the recent study not as a test of its validity, but as a framework for understanding the observations. In applying it, the fracture toughness, K_{Ic}; creep coefficient, B; and stress exponent, n, were all determined independently for the different silica ices.

In this study, we did not measure the coefficient of kinetic friction. The μ for most of materials ranges from 0 to 1. For example, the μ of granular water ice ranges from 0.02 to 1, depending on the sliding velocity and temperature; for review see *Schulson* [2016]. From equation (7), the sensitivity to μ is small compared to, for example, the sensitivity to K_{Ic}, n, and c.

3. Results

3.1. Stress-Strain Curve and Deformation Behavior

The ductile-to-brittle transition has been variously defined as, e.g., the loss of load bearing ability, the onset of dilatancy, or the localization of deformation along a fault. Here the deformation behavior, ductile or brittle, under compressive loading is characterized by the shape of the stress-strain curve and by the macroscopic appearance of the deformed material. In the case of ductile behavior of ice, the stress linearly increases with the strain at first, and then the slope of the curve gradually decreases, becomes zero, and then becomes negative; that is, the stress exhibits a rounded peak. After the negative sloped segment following the peak, the slope of the curve tends to level off and approach zero and the stress tends to become constant. Correspondingly, although internally damaged microscopically at the level of the grain size, cracks do not propagate and so macroscopic cracks do not develop. In the case of brittle behavior, the stress first increases linearly with the strain accompanied by some small stress drops, reaches a sharp peak, and then drops suddenly after terminal failure. Correspondingly, the ice fractures macroscopically.

Figure 3 shows the stress-strain curves for both pure ice and silica ices with $f = 0.06$ and 0.18 examined in this experiment. The other curves not shown in Figure 3 are shown in Figure S1 in the supporting information. As the strain rate increases, the stress-strain curves indicate a change from ductile behavior to brittle behavior as described in the preceding paragraph. At lower strain rates, all samples show ductile behavior, i.e., at strain rates lower than 10^{-4} s^{-1} for pure ice, $<10^{-3}$ s^{-1} for $f = 0.06$, and $<10^{-2}$ s^{-1} for $f = 0.18$. At higher strain rates, pure ice and silica ice with $f = 0.06$ show brittle behavior, i.e., at strain rates $>10^{-2}$ s^{-1} for pure ice and $>10^{-1}$ s^{-1} for $f = 0.06$. However, the stress-strain curve at the strain rate where the deformation behavior changes shows combined ductile and brittle character; the stress increases linearly at first and then reaches a maximum, but after the peak the stress decreases abruptly but does not drop suddenly to zero. This dual-like character is seen in the stress-strain curve for pure ice at 10^{-3} s^{-1}, for silica ice with $f = 0.06$ at 10^{-2} s^{-1}, and $f = 0.18$ at 10^{-1} and 5.7×10^{-1} s^{-1}. In the case of $f = 0.18$, the stress-strain curves remained ductile-like for all strain rates smaller than 6×10^{-1} s^{-1}. We did not strain at rates above this level owing to limitations in actuator velocity.

On stress-strain curves, the strain at the peak stress in the ductile regime and that in the brittle regime (the strain at failure) seems to be different in the case of pure ice from two previous works: the strain at the peak stress in the ductile regime was about 0.01 to 0.04 obtained by *Yasui and Arakawa* [2010] while that in the

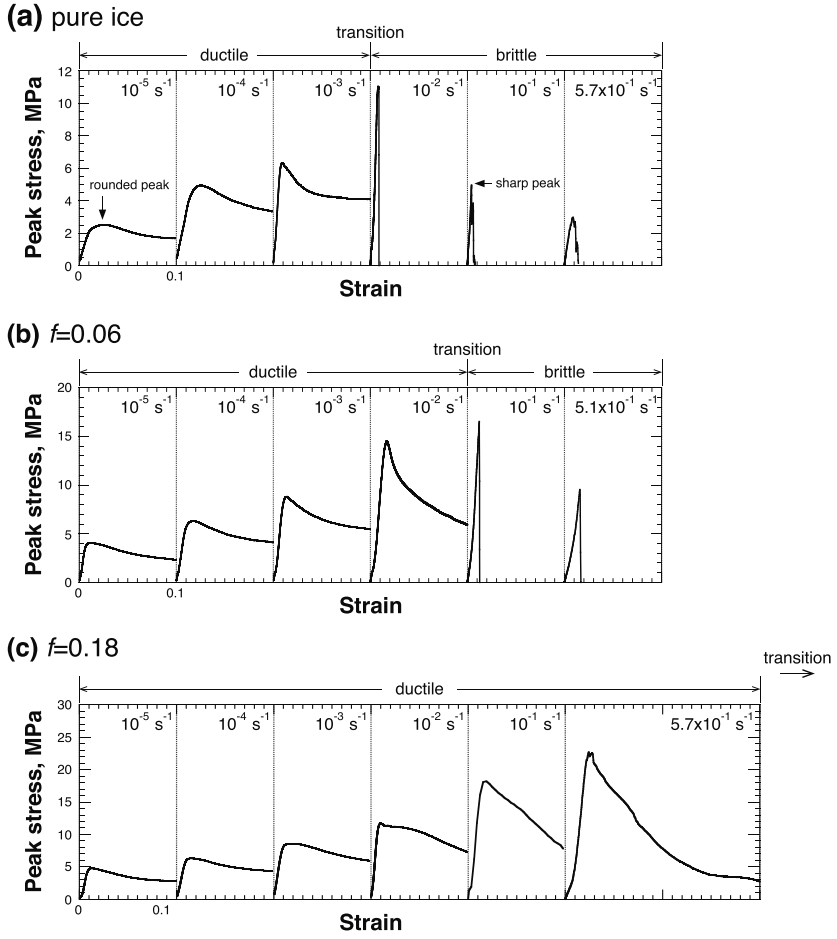

Figure 3. Stress-strain curves of (a) pure ice, (b) silica ice with silica volume fraction $f = 0.06$, and (c) silica ice with $f = 0.18$. The number on the upper right of each curve shows the strain rate. The curves on each figure is lined up in order of strain rate: the major division showing the grey line indicates the strain of 0.1 or 0.2, and the minor division showing the short line indicates the strain of 0.01, respectively. Three types of deformation (ductile, ductile-to-brittle transition, and brittle) show on the upper of each figure.

brittle regime was <0.003 [e.g., *Schulson*, 1990]. In the case of our pure ice, the strain at the peak stress on the stress-strain curve at the strain rate of 10^{-5} and 10^{-4} s^{-1}, which showed ductile character, was obtained to be 0.023–0.025, and it decreased to 0.007–0.008 at the strain rate of 10^{-3} s^{-1}. The strain at the peak stress at $>10^{-2}$ s^{-1}, which showed brittle character, was obtained to be 0.002–0.009, and it was smaller than that at the strain rate of $<10^{-4}$ s^{-1}, similar to previous works. On the other hand, in the case of silica ice for $f = 0.06$, the strain at the peak stress was almost consistent, irrespective of strain rate, 0.011–0.023. For $f = 0.18$, we could not observe the brittle behavior on stress-strain curves, but the strain at the peak stress was also consistent, irrespective of strain rate, 0.011–0.035. This behavior was different from that for pure ice.

The difference of the deformation behavior is also seen in the recovered samples after the test. Figure 4 shows photographs of samples recovered after compressing, either to an axial strain of 0.1 or 0.2 or to failure. The photographs correspond to the stress-strain curves of Figure 3. In the case of ductile behavior, the sample deformed either like a barrel where the central section was bulged or like a foot where the upper or lower part was bulged. These features are similar to those described by *Yasui and Arakawa* [2008, 2010]. The cause of barrel/foot heterogeneity was unknown in this study and was independent of sample setting method and sample preparation method. Furthermore, we performed duplicate compression tests under the same conditions. Bulges developed at different sites between different samples, although the stress-strain curves for the duplicate tests were almost identical, implying that the bulges did not affect the macroscopic compressive behavior. In the case of brittle behavior, the sample broke into many long pieces, owing to the

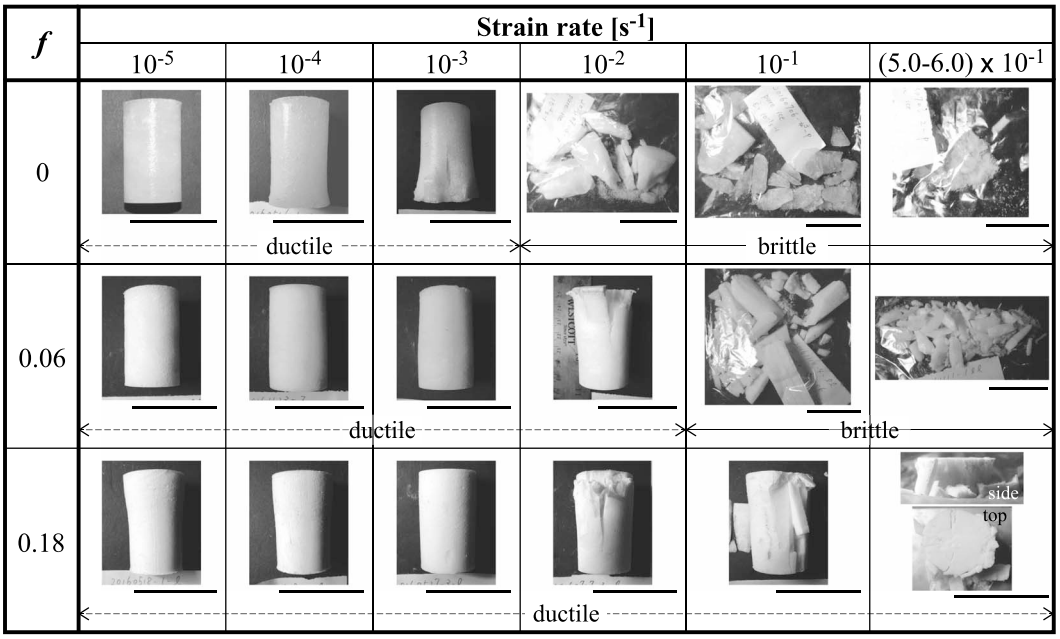

Figure 4. Images of recovered samples. The length of bar on each box indicates 50 mm.

development of macrocracks aligned along the axis of compression (i.e., due to axial splitting). At the transitional strain rate, that is, when the stress-strain curve shows the feature of both ductile and brittle behavior, large cracks were observed, but the sample did not break completely. These cracks were observed on the side surface of sample, and no cracks were observed in the center. For example, in the case of silica ice with $f = 0.18$, many large cracks were observed on the sample surface at 6×10^{-1} s^{-1}, but no cracks were found in the central part.

We thus found three types of deformation behavior from the obtained stress-strain curves and the recovered samples—ductile, transitional, and brittle. To identify the ductile-to-brittle transition more quantitatively, we used the criterion to distinguish between ductile and brittle behavior proposed by *Synder et al.* [2016]. They termed behavior to be brittle when the stress dropped to below one-half of the peak stress within an inelastic strain increment of 10^{-3} or smaller after the strain corresponding to the peak stress. When we used this criterion, the samples showing the transitional character were classified as ductile behavior, consistent with their remaining largely intact. The deformation behavior shown in Table 2 was determined from this criterion. We describe the results of peak stress in the next section in detail.

3.2. Peak Compressive Stress

Figures 5a–5c show the relationship between the peak stress and the strain rate. In the case of pure ice (Figure 5a) and silica ice of $f = 0.06$ (Figure 5b), the stress change with the strain rate was similar. At strain rates lower than the ductile-to-brittle transition, the peak stress increased by a power of $1/n$ with increasing strain rate. In this ductile region, the compressive strength can be described by the power law relationship, $\dot{\varepsilon} = B \cdot \sigma_{peak}{}^{n}$. The values for the constant B and the stress exponent n, as derived from Figure 5, are listed in Table 3. The values for pure ice were obtained by our results at strain rate smaller than 10^{-3} s^{-1} and the results by *Yasui and Arakawa* [2008]. The stress exponent, n, for $f = 0.06$ was approximately 2 times larger than that of pure ice. At the strain rate around the ductile-to-brittle transition, the slope decreased. At strain rates greater than the ductile-to-brittle transition, the peak stress decreased with increasing strain rate. The peak stress became larger as silica volume fraction increased. That the peak stress for silica ice with $f = 0.06$ reached a maximum at the ductile-to-brittle transition is similar to the behavior of pure ice [*Schulson and Duval*, 2009]. In the case of silica ice with $f = 0.18$ (Figure 5c), the peak stress continued to increase with increasing strain rate, because silica ice of this concentration did not show brittle behavior over the range of strain rate explored in this study. The values for the constant B and the stress exponent n for $f = 0.18$ are also listed in Table 3, and the n

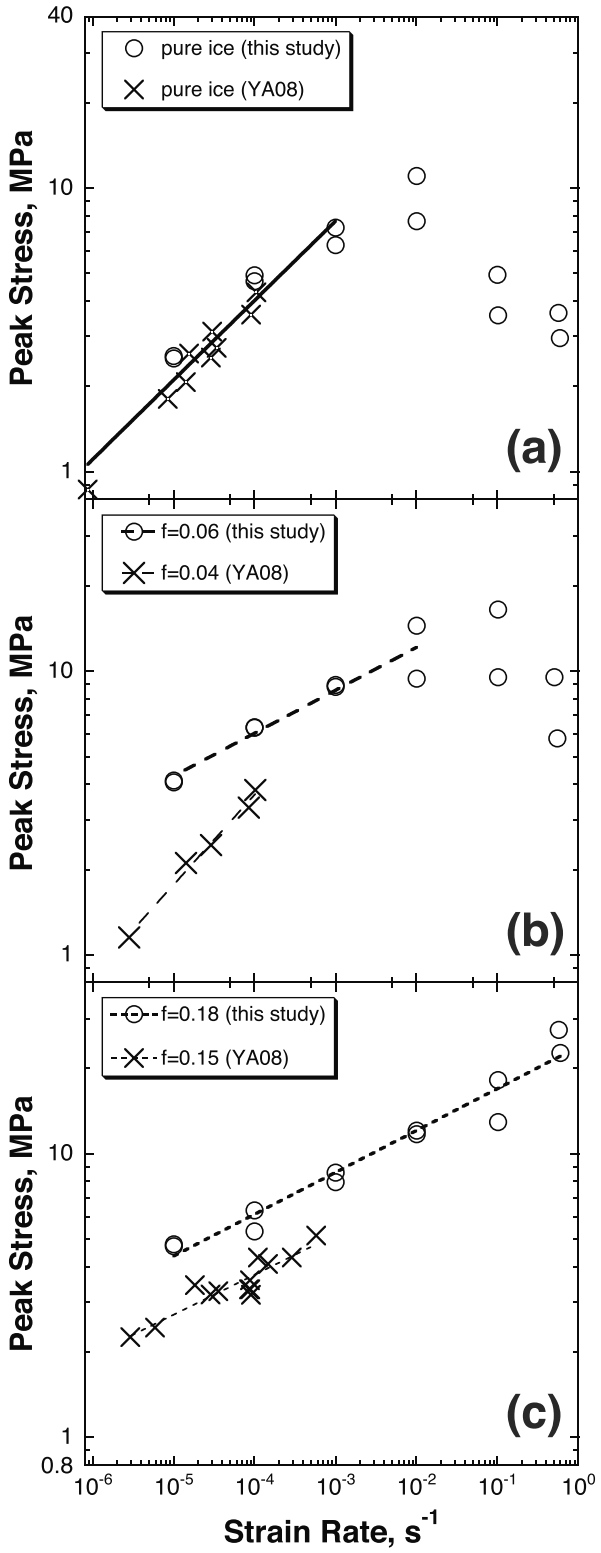

Figure 5. Peak stress versus strain rate for (a) pure ice, (b) silica ice with silica volume fraction $f = 0.06$, and (c) silica ice with $f = 0.18$. The "cross" symbols showing YA08 in each figure show the results of *Yasui and Arakawa* [2008]. The lines are fitted by $\dot{\varepsilon} = B \cdot \sigma_{peak}{}^{n}$ according to the least squares method, and that in Figure 5a is fitted by using our results in a ductile regime (strain rate smaller than 10^{-3} s^{-1}) and the results of *Yasui and Arakawa* [2008].

was almost constant with that for $f = 0.06$. Our results were compared with those obtained by *Yasui and Arakawa* [2008] (shown in Figure 5, labeled YA08). They also used pure ice and silica ices made using the same preparation method we used, but they used silica beads with a diameter of ~1 μm, 4 times larger than those used in this study. In the case of pure ice, their data and our new data are generally consistent with each other. In the case of silica ices, the silica volume fractions, f, of our silica ices differ somewhat from those of *Yasui and Arakawa* [2008]. Below we compare our results with those for $f = 0.04$ and 0.15, compared to our silica volume fractions of $f = 0.06$ and 0.18. In making this comparison, we found that the peak stress in the present study was about twice as large as that reported by *Yasui and Arakawa* [2008]. Furthermore, the stress exponent, n, is also larger, as listed in Table 3, particularly for the low-silica mixtures.

From Figure 5, the transitional strain rate, $\dot{\varepsilon}_{D/Bmeas}$, from our compression tests could be determined and values are listed in Table 4. We found that the $\dot{\varepsilon}_{D/Bmeas}$ increased with an increase in silica volume fraction.

3.3. Fracture Toughness and Elastic Properties

Figure 6 and Table 5 show the relationship between the fracture toughness, K_{Ic}, and the silica volume fraction. The average fracture toughness, K_{Ic_ave}, for pure ice in this study was 99.8 kPa $m^{1/2}$. This value is close to those of freshwater ice obtained in previous studies at −10°C [*Timco and Frederking*, 1986; *Nixon and Schulson*, 1987; *Wei et al.*, 1991] and serves as a validation of the procedure we used. As expected for a heterogeneous material, the values of K_{Ic} for each silica ice vary more than the fracture toughness of pure ice, yet the data shows clearly that K_{Ic}

Table 3. Constants B and n in the Power Law Describing Ductile Behavior, $\dot{\varepsilon} = B \cdot \sigma_{peak}{}^{n}$

Silica Volume Fraction f	B ($s^{-1}(MPa)^{-n}$)	n[c]
0 (this study and YA08)[a]	9.33×10^{-7}	3.31 (0.26)
0.06 (this study)	1.93×10^{-9}	6.08 (0.74)
0.18 (this study)	9.14×10^{-10}	6.48 (0.44)
0.04 (YA08[b])	1.70×10^{-6}	3.12 (0.18)
0.15 (YA08[b])	3.11×10^{-8}	6.05 (0.51)

[a]The B and the n are obtained from combining our data in a ductile regime with those of *Yasui and Arakawa* [2008].
[b]"YA08" represents the data of *Yasui and Arakawa* [2008].
[c]The numbers in parentheses give the standard deviation.

increases with silica volume fraction. We fit these data by a power function and obtained the best fitting equation (solid line, Figure 6):

$$K_{Ic}\left[\text{kPa m}^{1/2}\right] = (99.3 \pm 32.2) + (474.4 \pm 107.0) f^{0.44 \pm 0.15}. \quad (8)$$

Thus, we can say that the fracture toughness increases with increasing the silica volume fraction according to approximately the square root of silica volume fraction; i.e., $K_{Ic} \propto f^{0.5}$. The relationship between K_{Ic} and f is further discussed in section 4.1.

Figures 7a and 7b show the relationship between Young's modulus, E, and silica volume fraction for pure ice and silica ices. Young's modulus was calculated by using equation (1) and the average values of longitudinal and shear velocities, V_l and V_s, shown in Table 6. All data are shown in Table S1 in the supporting information. The E of our pure ice was 8.7 GPa, a little smaller than typical Young's modulus of 9.3 GPa for polycrystalline granular ice at −10°C [*Schulson and Duval*, 2009]. This difference is likely caused by the small amount of porosity that was present. *Gibson and Ashby* [1988] defined the relationship between Young's modulus, E, and the density, ρ, for snow as $E_{snow}/E_{ice} = (\rho_{snow}/\rho_{ice})^2$. Furthermore, *Yasui and Arakawa* [2010] also examined the dependence of E on porosity, ϕ, in pure ice and obtained the empirical equation, E [GPa] = 9.1 − 0.19ϕ, for pure ice ($0 \le \phi$ [%] ≤ 20). Our pure ice had a porosity of 3–5%, indicating a Young's modulus of our pure ice specimens to be 8.4–8.8 GPa from the relationship of *Gibson and Ashby* [1988] and 8.2–8.5 GPa from the empirical equation of *Yasui and Arakawa* [2010]. These calculated values are very close to our experimentally obtained value, 8.7 GPa.

Figure 7a shows the relationship between Young's modulus, E, and silica volume fraction over the range of f explored in these experiments. The values of E of silica ices are larger than that of pure ice, and furthermore, E increased approximately linearly with the silica volume fraction over the range explored here. The data for E can fit by a linear function as E [GPa] = 9.3 + 25.1f ($0 \le f \le 0.34$). Figure 7b shows the same experimental data in Figure 7a along with the data for amorphous silica glass (f = 1) at 20°C with a density 2200 kg m^{-3} [*Pabst and Gregorová*, 2013]. If we include this point in the overall picture, the variation in E with silica volume fraction is bounded by the Voigt upper bound and by the Reuss lower bound of a mixture of phases [e.g., *Watt et al.*, 1976]. The Voigt model, M_V, and the Reuss model, M_R, are expressed as follows:

$$M_V = \sum_{i=1}^{N} f_i M_i, \quad (9)$$

$$\frac{1}{M_R} = \sum_{i=1}^{N} \frac{f_i}{M_i}, \quad (10)$$

Table 4. Critical Transitional Strain Rate at Ductile-to-Brittle Transition Determined From the Compression Tests, $\dot{\varepsilon}_{D/Bmeas}$, and From the Calculation of Equation (7), $\dot{\varepsilon}_{D/Bcal}$

Silica Volume Fraction f	$\dot{\varepsilon}_{D/Bmeas}$ (s^{-1})	$\dot{\varepsilon}_{D/Bcal}$ (s^{-1})
0	10^{-3}–10^{-2}	2×10^{-3}–4×10^{-2}
0.06	10^{-2}–10^{-1}	2×10^{-1}–4×10^{2}
0.18	$>6 \times 10^{-1}$	2×10^{1}–7×10^{3}

where f_i is the volume fraction of the ith constituent phase and M_i is the elastic modulus of the ith constituent phase. The average of the Voigt and Reuss models, M_{VRH} [*Hill*, 1952], is expressed as follows:

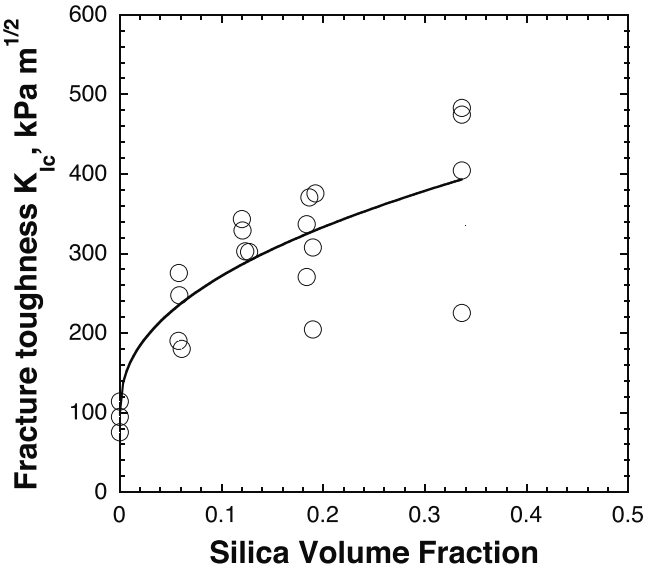

Figure 6. Fracture toughness versus silica volume fraction. The solid line is fitted by equation (8).

$$M_{VRH} = \frac{M_V + M_R}{2}, \quad (11)$$

and describes the data reasonably well.

Poisson's ratios, ν, which were calculated by using equation (2), of pure ice and silica ices were almost the same, irrespective of silica volume fraction (Table 6). The average value was 0.327 ± 0.019. This value is also consistent with that of the randomly oriented polycrystalline granular ice at −5°C, 0.33 [*Schulson and Duval*, 2009]. For reference, Poisson's ratio of $f = 1$, that is, of silica glass is $\nu = 0.168$ [*Pabst and Gregorová*, 2013], about one-half that of ice. However, the Poisson's ratio of pure silica beads, rather than intact silica glass, is unknown.

4. Discussion

4.1. Relationship Between Fracture Toughness and Elastic Properties

Fracture toughness, K_{Ic}, is related to Young's modulus, E, and to Poisson's ratio, ν, as follows:

$$K_{Ic} = \sqrt{G_c \cdot E'}, \quad (12)$$

where G_c is the critical value of the crack-extension force (or the strain energy release rate) for mode-I loading and E' is expressed as

$$E' = \frac{E}{1-\nu^2}. \quad (13)$$

In section 3.3, we found that E increased linearly upon increasing the silica volume fraction; that is, $E \propto f$ and that ν was almost independent of silica volume fraction, ~0.33, over the range of f explored here. From these results and equation (13), the parameter, E', also increases upon increasing the silica volume fraction; i.e., $E' \sim 1.1E \propto f$. Thus, given equation (12), and assuming that the crack-extension force, G_c, is relatively independent of silica volume fraction over the range of f explored, we expect fracture toughness to scale with the square root of the silica volume fraction, $K_{Ic} \propto f^{0.5}$. This relationship is in good agreement with the experimental observations (Figure 6), indicating that the increase in fracture toughness with silica volume fraction primarily results from the linear increase in Young's modulus with silica volume fraction.

Table 5. Average Fracture Toughness, K_{Ic_ave}, for Pure Ice and Silica Ices

Silica Volume Fraction f	K_{Ic_ave}[a] (kPa m$^{1/2}$)
0	99.8 (18.5)
0.06	223.6 (45.7)
0.12	316.1 (23.7)
0.18	311.1 (65.4)
0.34	396.9 (119.6)

[a]The numbers in parentheses give the standard deviation.

4.2. Microstructure and Ductile Behavior of Ice-Silica Mixtures

As described in section 3.2, within the ductile regime, the peak strengths for silica ices are greater than that for pure ice but are almost constant between $f = 0.06$ and $f = 0.18$. The reason

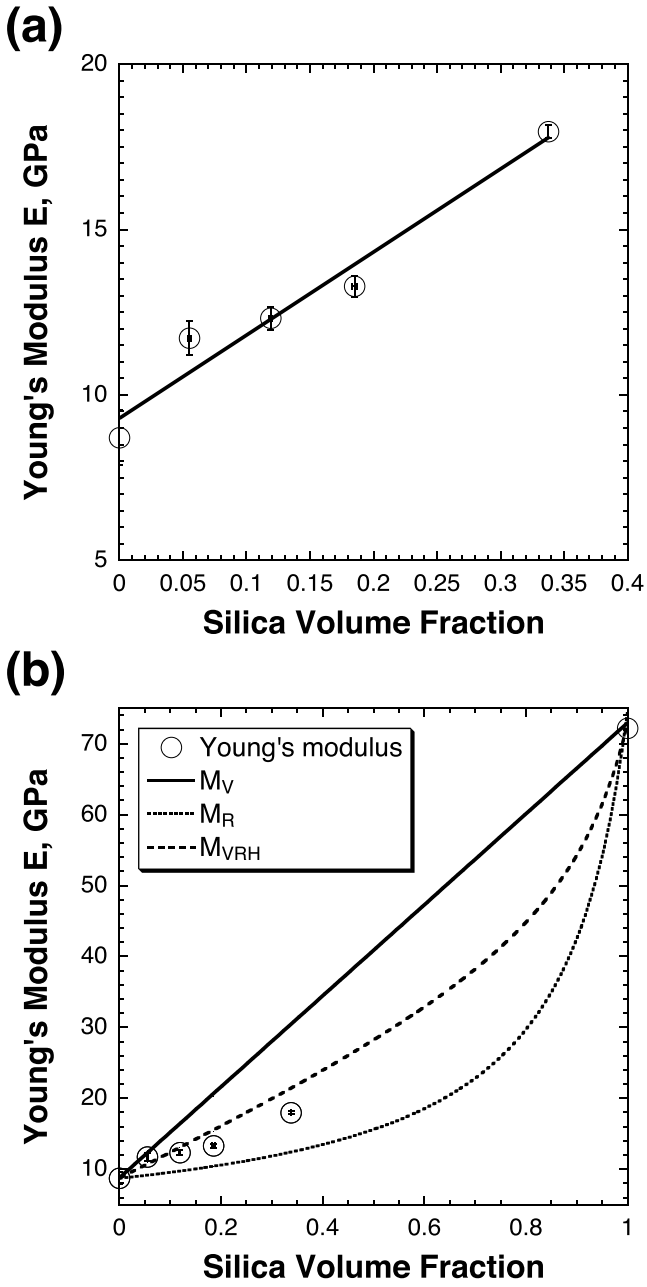

Figure 7. Young's modulus versus silica volume fraction. (a) The range explored in this experiments. The solid line is fitted by the linear function at the silica volume fraction from 0 to 0.34. (b) The extended figure of both axes to include the $f = 1$ data. The three lines represent the functions determined by equations (9)–(11).

the peak stress for silica ices became larger than that for pure ice might be explained by the difference in microstructure. As shown in Figure 1, in the presence of silica the ice grains tend to be immersed within a relatively fine composite matrix composed of silica beads and frozen water. This composite, we expect, is stronger than pure ice. This strengthening effect of the silica/ice composite is also obvious from the results obtained in *Yasui and Arakawa* [2008]; they found that the peak stress was greater as silica beads volume fraction increased over the range of f from 0.04 to 0.63 in the ductile regime. At a more fundamental level, the silica-induced strengthening, particularly of the finely structured ice/silica matrix, might be explicable in terms of dislocation-particle interactions, in an Orowan manner (for a review of this mechanism, see *Brown and Ham* [1971]).

We also compared our experimental results with those of *Yasui and Arakawa* [2008], who used ice-1-μm silica bead mixtures with silica volume fraction of $f = 0$, 0.04, and 0.15. We found that our compressive strengths were higher than those for *Yasui and Arakawa* [2008]. This might also be explained by using Orowan mechanism. Owing to their mechanism, one possible explanation for the greater strength in the present material relates to the smaller bead size, for that mechanism dictates that, for a given volume fraction, particle-induced strengthening is inversely proportional to particle diameter. A rough calculation based upon the bowing of dislocations between particles leads to strengthening given by the relationship $G\bar{b}/L$ (where G is shear modulus, $\bar{b}$ is dislocation Burgers vector, and L is average spacing between particles). As an example calculation, we used $\bar{b} = 3 \times 10^{-10}$ m [*Fukuda et al.*, 1987] and values of G from our ultrasound velocity measurements as shown in equation (3) (these values are listed in Table 6 with the other elastic properties). If we assume that the particles are distributed homogeneously over a whole sample, then L equals $(4\pi/3f)^{1/2}r$ (where r is particle radius). In that case, the expected strengthening would be around 0.6 MPa for $f = 0.06$ for 0.25 μm particles, 1 order of magnitude smaller than the present observation. However, from Figure 1 it is clear that the silica beads in our silica ices are not distributed randomly, but rather dispersed as a fine composite in which pure ice is immersed. This means that the interparticle spacing is smaller than estimated assuming that the particles are homogeneously distributed. If we assume that the effective value of L is of the same magnitude as particle size, r, then we estimate the

strengthening to be around 5 MPa for $f = 0.06$ for 0.25 μm particles, in order-of-magnitude agreement with the present observations. Furthermore, if we calculate the strengthening stress $G\bar{b}/r$ for our silica ices of $f = 0.06$ and 0.18, then we can explain their peak strengths being consistent with each other in the ductile regime because the $G\bar{b}/r$ is independent of silica volume fraction f when we assume $L \sim r$, i.e., that the particles are dispersed in a fine matrix. To more robustly clarify the nature of the difference between the earlier and the present results, more work is needed using different silica bead sizes.

Furthermore, as already described in sections 3.1 and 3.2, we found that the experimental transitional strain rate, $\dot{\varepsilon}_{D/Bmeas}$, increased with increasing the silica volume fraction. This might be caused by the microstructure of silica ices. As shown in Figure 1, in the silica ices the ice grains/seeds are surrounded by the fine composite matrix composed of silica beads and frozen water. Because of the fine grain size, we expect that this composite is strong compared with ice grains/seeds due to particle-induced strengthening and the inhibition of the initiation of cracks.

4.3. Ductile-to-Brittle Transition of Pure Ice

We obtained from our experiments the transitional strain rate, $\dot{\varepsilon}_{D/Bmeas}$, of pure ice of 10^{-3}–10^{-2} s^{-1}. This range is consistent with previous estimates. *Arakawa and Maeno* [1997] examined the transitional strain rate of pure polycrystalline granular ice with ice grain size of 0.9 mm at temperatures from −10 to −173°C. They determined the transitional strain rate at −10°C to be 10^{-2} s^{-1}. According to compiled data by *Gold* [1977], the transitional strain rate of pure polycrystalline ice at −10°C is 10^{-3} s^{-1}. *Arakawa and Maeno* [1997] suggested that their higher value of $\dot{\varepsilon}_{D/B}$ compared with Gold's value might be caused by confinement; their samples were slightly confined at both ends due to their setting method, and this effect caused the enhancement of transitional strain rate [*Schulson and Buck*, 1995]. *Batto and Schulson* [1993] examined the transitional strain rate of columnar-grained freshwater ice at −10°C under unconfined compression loading. The specimens were compressed across the columns. They found that the transitional strain rate for ice of grain size of 3.5 mm was 3×10^{-4} s^{-1}, 1 order of magnitude greater than that ($3–6 \times 10^{-5}$ s^{-1}) of ice with 15 mm grains. They concluded that the transitional strain rate could be scaled as $(\text{grain size})^{-1.5}$. Using this scaling, Gold's value (10^{-3} s^{-1}) for a grain size of ~1 mm is slightly smaller than that for *Arakawa and Maeno* [1997]. *Golding et al.* [2013] examined the transitional strain rate of columnar-grained freshwater ice with the ice grain size of 3–6 mm at −10°C, and they obtained the transitional strain rate as 10^{-4} s^{-1}, consistent with the data interpolated by using the experimental function of *Batto and Schulson* [1993].

Our obtained $\dot{\varepsilon}_{D/Bmeas}$ of pure ice with the ice grain size of 0.3–0.4 mm (section 2.2) is also consistent with the value obtained by the interpolation of experimental function of *Batto and Schulson* [1993]. From these results, we can say that the transitional strain rate of pure ice depends on the ice grain size and that transitional strain rate is independent of the structure of ice, that is, whether the microstructure is granular or columnar.

4.4. Theoretical and Experimental Critical Transitional Strain Rate of Silica Ice

The transitional strain rate, $\dot{\varepsilon}_{D/Bcal}$, predicted by equation (7), as explained in section 2.5 requires the half length of initial crack, c, and the coefficient of friction, μ. Here we estimate c as the average ice grain radius within the sample [*Schulson and Duval*, 2009]. We used for c the half-length of the major axis corresponding to the peak of the frequency distribution. Thus, we used the values $c = 0.23$ mm for pure ice, and $c = 0.18$ mm for $f = 0.06$ and $c = 0.15$ mm for $f = 0.18$. We did not determine the coefficient of friction experimentally, so we estimated it from previous work. The coefficient of friction is known to depend on temperature and sliding velocity [e.g., *Maeno et al.*, 2003; *Schulson and Fortt*, 2012; *Golding et al.*, 2013; *Schulson*, 2016]. For example, *Schulson and Fortt* [2012] reported that the value of μ (as determined from the slope of curves showing shear stress versus normal stress during sliding and not from the ratio of shear stress to normal stress) increased with increasing sliding velocity at lower sliding velocity while it decreased at higher sliding velocity at temperature of −10°C. Here we chose the coefficient of friction for pure ice from the results of ice-ice friction obtained by *Schulson and Fortt* [2012] at sliding velocities estimated as $\dot{\varepsilon}_{D/Bmeas}$ multiplied by the value of c, following *Golding et al.* [2013]. Specifically, we assume that the μ of pure ice is 0.35–0.5 at sliding velocities of 2×10^{-7}–2×10^{-6} m s^{-1}. In the case of silica ices, we used the μ between a block of ice-debris mixture and a rock block obtained by *Zoet et al.* [2013]. They used a block of ice-debris mixture with a debris grain size less than 1.25 mm and a debris mass content

Table 6. Longitudinal and Shear Velocities, V_l and V_s, and Elastic Moduli (Young's Modulus, E; Poisson's Ratio, ν; and Shear Modulus, G) of Pure Ice and Silica Ices (Average)

Silica Volume Fraction f	Longitudinal Velocity V_l[a] (m s^{-1})	Shear Velocity V_s[a] (m s^{-1})	Young's Modulus E[a] (GPa)	Poisson's Ratio ν[a]	Shear Modulus G[a] (GPa)
0	3661.4 (218.4)	1950.3 (103.1)	8.71 (0.83)	0.30 (0.004)	3.34 (0.31)
0.06	4396.1 (23.2)	2132.6 (58.5)	11.72 (0.52)	0.35 (0.01)	4.35 (0.23)
0.12	4309.3 (3.0)	2094.9 (49.2)	12.32 (0.35)	0.35 (0.01)	4.58 (0.16)
0.18	4190.1 (59.8)	2117.8 (29.7)	13.28 (0.31)	0.33 (0.0001)	5.00 (0.12)
0.34	4344.0 (111.8)	2255.6 (18.7)	17.97 (0.19)	0.32 (0.009)	6.83 (0.03)
1[b]	–	–	72.2	0.168	–

[a]The numbers in parentheses give the standard deviation.
[b]Young's modulus E and Poisson's ratio ν of $f = 1$ are values of amorphous silica glass referred from *Pabst and Gregorová* [2013].

of 0–50%, and the sliding velocity was 10^{-5} m s^{-1}. From the calculation of sliding velocity by *Golding et al.* [2013], the sliding velocity for $f = 0.06$ is 2×10^{-6}–2×10^{-5} m s^{-1}. In the case of silica ice with $f = 0.18$ we could not obtain an accurate estimate $\dot{\varepsilon}_{D/Bmeas}$, so in this calculation, we approximated $\dot{\varepsilon}_{D/Bcal}$ using the highest strain rate, 6×10^{-1} s^{-1}. Thus, for $f = 0.18$ the sliding velocity is $>9 \times 10^{-5}$ m s^{-1}. These sliding velocities for $f = 0.06$ and 0.18 are close to that by *Zoet et al.* [2013]. They did not measure the μ at −10°C, so we used their data at a temperature of −6°C, nearest our experiments. From their data, the μ for $f = 0.06$ is 0.48 and that for $f = 0.18$ is 0.65. It should be noted from equation (7) that the calculated value of the transitional strain rate depends on the term $1/(1 - \mu)$ and so, over the range of friction coefficient just noted, is not highly dependent on the value of this parameter. The other parameters needed to calculate $\dot{\varepsilon}_{D/Bcal}$ are shown in Tables 3 and 5. Summarized in Table 4 are the calculated values of transitional strain rate, $\dot{\varepsilon}_{D/Bcal}$, obtained by using the equation (7) and by taking into account the standard deviations of n and K_{Ic} listed in Tables 3 and 5.

The calculated transitional strain rates, $\dot{\varepsilon}_{D/Bcal}$, increase with increasing silica volume fraction. This behavior was consistent with that of $\dot{\varepsilon}_{D/Bmeas}$ obtained in our experiments. Under the assumptions of the model, this increase might be caused by the sensitivity of $\dot{\varepsilon}_{D/B}$ to the stress exponent, n, and fracture toughness, K_{Ic}. That is, both n and K_{Ic} increase with increasing silica volume fraction. In the case of $f = 0.18$, both n and K_{Ic} are 2.5–3 times larger than those of pure ice. The $\dot{\varepsilon}_{D/Bcal}$ includes the term of $K_{Ic}^{\ n}$ so this term significantly affects the calculated increase of $\dot{\varepsilon}_{D/Bcal}$.

The $\dot{\varepsilon}_{D/Bcal}$ of pure ice was in good agreement with the measured value $\dot{\varepsilon}_{D/Bmeas}$. For the silica ice of $f = 0.06$, the $\dot{\varepsilon}_{D/Bcal}$ was larger than the $\dot{\varepsilon}_{D/Bmeas}$, although the lower end of the calculated range was close to the measured transitional rate. For the silica ice of $f = 0.18$, although a range of 3 orders of magnitude in strain rate was calculated, comparison between calculated and measured values is difficult because a transition was not observed at the highest strain rate (6×10^{-1} s^{-1}) explored here. We caution that there is uncertainty in these calculated values for the silica ices. The uncertainty arises from uncertainty in the c-values and from the high sensitivity of the transitional strain rate to the exponent n. Unfortunately, in silica ice, owing to its opacity, it is difficult to observe the initial crack length. In this calculation, we assumed that the c was equal to the half-length of major axis of original ice grains/seeds. However, as the silica volume fraction increases, the area of fine composite matrix surrounding original ice seeds increases and ice grains tend to separate from each other as shown in Figure 1. Therefore, as the silica volume fraction increases, this matrix is expected to play an increasing role as a framework in the silica ice, similar to columns in a building. It is unclear how to adjust the effective c-value to account for this. The important point, though, is that even if the range of standard deviation of K_{Ic} and n is small, the range of $K_{Ic}^{\ n}/c^{n/2}$ will be large.

In previous work little attention has been given to the effect of hard particles such as silica beads on the ductile-to-brittle transition. *Yasui and Arakawa* [2008] examined the transitional strain rate of ice-silica-bead mixtures with silica volume fraction of 0.29 and 0.63 and found that it was rather low; i.e., ~2×10^{-4} s^{-1}, much smaller than our $\dot{\varepsilon}_{D/Bmeas}$ of $>6.0 \times 10^{-1}$ s^{-1} for $f = 0.18$. Their result would thus appear to be in contradiction with the results of this study where $\dot{\varepsilon}_{D/Bmeas}$ was found to increase with increasing the silica volume fraction. However, the resolution of this difference probably resides in the variation in the parameter, B, of

equation (7). *Yasui and Arakawa* [2008] concluded that B exponentially decreased with increasing the silica volume fraction for f greater than 0.15. On the other hand, for f greater than 0.15, the stress exponent, n, while higher than that of pure ice, remained almost constant at ~6–7 at silica volume fraction of 0.15–0.63. If these relationships can be applied to the results of our silica ices, then $\dot{\varepsilon}_{D/Bcal}$ first increases with increasing the silica volume fraction owing to an increase in n and K_{Ic}, and then decreases for $f > 0.18$ as B decreases exponentially with increasing the silica volume fraction. Therefore, it is expected that the critical transitional strain rate reaches a maximum at an intermediate silica volume fraction.

We note again that we applied the Schulson-Renshaw model of the ductile-brittle transition only as a framework for understanding the behavior of silica-rich ice, not as a test of its validity. For such material, as is now apparent, the model works less well than it does for pure ice, possibly because it is incomplete (missing are the primary and tertiary stages of creep) and possibly because it does not include the microstructural complexity introduced by the presence of hard particles. So we have to include in the model a possible effect of the distribution of ice seeds and silica particles versus the silica volume fraction.

From the perspective of the rheological behavior of icy planetary bodies, it is clear from the results of the present study and of the earlier work of *Yasui and Arakawa* [2008] that silica dust plays a major role in the ductile to brittle transition. Moreover, its effect is not a monotonic one, at least in relatively warm mixtures. Such compacted behavior is expected to affect tectonic style that is reflected, for example, in both the grooved light terrain and the heavily cratered dark terrain of Ganymede. Hopefully, the new results will be of use to planetary modelers.

5. Summary and Conclusions

We performed unconfined compression experiments on ice-0.25-μm-silica bead mixtures with silica volume fraction of 0, 0.12, and 0.18 at a temperature of −10°C and a strain rate from 10^{-5} to 6.0×10^{-1} s^{-1} to examine the effect of silica beads on the ductile-to-brittle transition. Furthermore, we measured the fracture toughness and elastic moduli of the mixtures at silica volume fractions from 0 to 0.34. We summarize our results and conclusions as follows:

1. Over the range of silica volume fraction considered ($0 \le f \le 0.34$), fracture toughness, K_{Ic}, measured by three-point bending tests, was found to increase with increasing silica volume fraction, f, and it scaled with the square root of silica volume fraction; i.e., $K_{Ic} \propto f^{0.5}$. Young's modulus, E, increased linearly with increasing silica volume fraction, $E \propto f$, while Poisson's ratio, ν, was almost the same, ~0.33, essentially independent of silica volume fraction over the range of f explored.
2. The transitional strain rate, $\dot{\varepsilon}_{D/Bmeas}$, was determined from the character of the stress-strain curve, from the recovered sample appearance and from the peak stress on the stress-strain curve, and was found to be 10^{-3}–10^{-2} s^{-1} for pure ice, 10^{-2}–10^{-1} s^{-1} for $f = 0.06$, and $>6 \times 10^{-1}$ s^{-1} for $f = 0.18$. Over the range explored in these experiments ($0 \le f \le 0.18$), the $\dot{\varepsilon}_{D/Bmeas}$ increased with increasing silica volume fraction.
3. We analyzed our experimental results within the framework of the physical model of transitional strain rate proposed by *Schulson* [1990] and *Renshaw and Schulson* [2001]. In the case of pure ice, the calculated transitional strain rate was consistent with the measured value in our experiments. In the case of silica ices for $f = 0.06$ and 0.18, the calculated transitional strain rate was larger than that measured in our experiments and had significant uncertainty. Within the context of the model, this difference is attributed to uncertainties in the initial crack length, c. As a result, we could not determine the transitional strain rate of silica ices with certainty using the physical model. The transitional strain rate for $f = 0.29$ and 0.63, obtained by *Yasui and Arakawa* [2008], was smaller than those of our silica ices for $f = 0.06$ and 0.18, owing most likely to the exponential decrease of B with increasing silica volume fraction and implying that the transition strain rate of ice-silica mixtures loaded under uniaxial compression at −10°C reaches a maximum at a silica volume fraction between 0.18 and 0.29.

Acknowledgments
The authors acknowledge the advice and help of Daniel Iliescu and Charles P. Daghlian. Experimental techniques, data, and results presented in this paper are available in all tables and figures shown here, in the supporting information, and references. This work was partially supported by funding from the National Science Foundation (EAR-1519706), by the George Austin Colligan Professorship at Dartmouth and by Kobe University Long Term Overseas Visit Program for Young Researchers. Finally, the authors would like to thank Brian Evans and an anonymous reviewer for their very helpful comments and availability during the review stages.

References

Arakawa, M., and N. Maeno (1997), Mechanical strength of polycrystalline ice under uniaxial compression, *Cold Reg. Sci. Technol.*, *26*, 215–229.
ASTM E399 (2009), Standard test method for plane-strain fracture toughness of metallic materials, American Society for Testing and Materials.
Batto, R. A., and E. M. Schulson (1993), On the ductile-to-brittle transition in ice under compression, *Acta Metall. Mater.*, *41*(7), 2219–2225.
Brown, L. M., and R. K. Ham (1971), Dislocation-particle interaction, in *Strengthening Methods in Crystals*, edited by A. Kelly and R. B. Nicholson, pp. 9–135, Elsevier, New York.

De Sanctis, M. C., et al. (2015), Ammoniated phyllosilicates with a likely outer solar system origin on (1) Ceres, *Nature*, *528*, 241–244.
Dombard, A. J., and W. B. McKinnon (2006), Folding of Europa's icy lithosphere: An analysis of viscous-plastic buckling and subsequent topographic relaxation, *J. Struct. Geol.*, *28*, 2259–2269.
Durham, W. B., H. C. Heard, and S. H. Kirby (1983), Experimental deformation of polycrystalline H_2O ice at high pressure and low temperature: Preliminary results, *J. Geophys. Res.*, *88*, 377–392.
Durham, W. B., S. H. Kirby, and L. A. Stern (1992), Effects of dispersed particulates on the rheology of water ice at planetary conditions, *J. Geophys. Res.*, *97*(E12), 20,883–20,897.
Durham, W. B., A. V. Pathare, L. A. Stern, and H. J. Lenferink (2009), Mobility of ice sand packs, with application to Martian permafrost, *Geophys. Res. Lett.*, *36*, L23203, doi:10.1029/2009GL040392.
Fukuda, A., T. Hondoh, and A. Higashi (1987), Dislocation mechanisms of plastic deformation of ice, *J. Phys. Colloq.*, *48*(C1), C1-163–C1-173.
Gibson, L. G., and M. F. Ashby (1988), *Cellular Solids: Structure and Properties*, 1st ed., p. 357, Pergamon Press, Oxford.
Gold, L. W. (1977), Engineering properties of fresh-water ice, *J. Glaciol.*, *81*, 197–212.
Golding, N., C. E. Burks, K. N. Lucas, A. L. Fortt, S. A. Synder, and E. M. Schulson (2013), Mechanical properties of the ice I-magnesium sulfate eutectic: A comparison with freshwater ice in reference to Europa, *Icarus*, *225*, 248–256.
Hill, R. (1952), The elastic behavior of crystalline aggregate, *Proc. Phys. Soc. London, Sect. A*, *65*, 349–354.
Kirby, S. H., W. B. Durham, and H. C. Head (1985), Rheologies of H_2O ices Ih, II, and III at high pressures: A progress report, in *Ices in the Solar System*, edited by J. Klinger et al., pp. 89–107, D. Reidel, Dordrecht, Netherlands.
Maeno, N., M. Arakawa, A. Yasutome, N. Mizukami, and S. Kanazawa (2003), Ice-ice friction measurements, and water lubrication and adhesion-shear mechanisms, *Can. J. Phys.*, *81*, 241–249, doi:10.1139/P03-023.
Mangold, N., P. Allemand, P. Duval, Y. Geraud, and P. Thomas (2002), Experimental and theoretical deformation of ice-rock mixtures: Implications on rheology and ice content of Martian permafrost, *Planet. Space Sci.*, *50*, 385–401.
McCord, T. B., and C. Sotin (2005), Ceres: Evolution and current state, *J. Geophys. Res.*, *110*, E05009, doi:10.1029/2004JE002244.
Moore, P. L. (2014), Deformation of debris-ice mixtures, *Rev. Geophys.*, *52*, 435–467, doi:10.1002/2014RG000453.
Nimmo, F. (2004), Dynamics and rifting and modes of extension on icy satellites, *J. Geophys. Res.*, *109*, E01003, doi:10.1029/2003JE002168.
Nixon, W. A., and E. M. Schulson (1987), A micromechanical view of the fracture toughness of ice, *J. Phys.*, *48*, 313–319.
Pabst, W., and E. Gregorová (2013), Elastic properties of silica polymorphs—A review, *J. Ceram. -Silikáty*, *57*(3), 167–184.
Qi, S., and E. M. Schulson (1998), The effect of temperature on the ductile-to-brittle transition in columnar ice, 14th Int. Symp. on Ice, Clarkson Univ., A. A. Balkema Publ., Potsdam, New York.
Renshaw, C. E., and E. M. Schulson (2001), Universal behaviour in compressive failure of brittle materials, *Nature*, *412*, 897–900, doi:10.1038/35091045.
Schulson, E. M. (1990), The brittle compressive fracture of ice, *Acta Metall. Mater.*, *38*, 1963–1976.
Schulson, E. M. (2004), Compressive shear faults within arctic sea ice: Fracture on scales large and small, *J. Geophys. Res.*, *109*, C07016, doi:10.1029/2003JC002108.
Schulson, E. M. (2016), Low-speed friction and brittle compressive failure of ice: Fundamental processes in ice mechanics, *Int. Mater. Rev.*, *60*(8), 451–478, doi:10.1179/1743280415Y.0000000010.
Schulson, E. M., and E. Buck (1995), The ductile-to-brittle transition and ductile failure envelopes of orthotropic ice under biaxial compression, *Acta Metall. Mater.*, *43*, 3661–3668.
Schulson, E. M., and P. Duval (2009), *Creep and Fracture of Ice*, p. 401, Cambridge Univ. Press, Cambridge.
Schulson, E. M., and A. L. Fortt (2012), Friction of ice on ice, *J. Geophys. Res.*, *117*, B12204, doi:10.1029/2012JB009219.
Squyres, S. W. (1989), Urey prize lecture: Water on Mars, *Icarus*, *79*, 229–288.
Synder, S. A., E. M. Schulson, and C. E. Renshaw (2016), Effects of prestrain on the ductile-to-brittle transition of ice, *Acta Mater.*, *108*, 110–127.
Thomas, P. C. (2010), Sizes, shapes, and derived properties of the saturnian satellites after the Cassini nominal mission, *Icarus*, *208*, 395–401.
Timco, G. W., and R. M. W. Frederking (1986), The effects of anisotropy and microcracks on the fracture toughness of freshwater ice, Proc. 5th Int. Offshore Mechan. Arctic Eng. (OMAE) Symp., Tokyo, vol. 4, edited by V. J. Lunardini et al., pp. 341–348, Am. Soc. Mech. Eng., New York.
Watt, J. P., G. F. Davies, and R. J. O'Connell (1976), The elastic properties of composite materials, *Rev. Geophys. Space Phys.*, *14*, 541–562.
Wei, Y., S. J. DeFranco, and J. P. Dempsey (1991), Crack-fabrication techniques and their effects on the fracture toughness and CTOD for fresh-water columnar ice, *J. Glaciol.*, *37*, 270–280.
Yasui, M., and M. Arakawa (2008), Experimental study on the rate dependent strength of ice-silica mixture with silica volume fractions up to 0.63, *Geophys. Res. Lett.*, *35*, L12206, doi:10.1029/2008GL033787.
Yasui, M., and M. Arakawa (2010), Rate-dependent strength of porous ice-silica mixtures and its implications for the shape of small to middle-sized icy satellites, *Icarus*, *210*, 956–967.
Zoet, L. K., B. Carpenter, M. Scuderi, R. B. Alley, S. Anandakrishnan, C. Marone, and M. Jackson (2013), The effects of entrained debris on the basal sliding stability of a glacier, *J. Geophys. Res. Earth Surf.*, *118*, 1–11, doi:10.1002/jgrf.20052.